MTLA 38 (2024) 102241

Contents lists available at ScienceDirect

Materialia

journal homepage: www.elsevier.com/locate/mtla

Laser energy-dependent processability of non-equiatomic TiNbMoTaW high-entropy alloy through in-situ alloying of elemental feedstock powders by laser powder bed fusion

Yong Seong Kim [a], Ozkan Gokcekaya [a,b], Aira Matsugaki [a,b], Ryosuke Ozasa [a,b], Takayoshi Nakano [a,b,*]

[a] Division of Materials and Manufacturing Science, Graduate School of Engineering, Osaka University, 2-1, Yamadaoka, Suita, Osaka 565-0871, Japan
[b] Anisotropic Design and Additive Manufacturing Research Center, Osaka University, 2-1, Yamadaoka, Suita, Osaka 565-0871, Japan

ARTICLE INFO

Keywords:
High entropy alloys
Additive manufacturing
In-situ alloying
Segregation
Cracking

ABSTRACT

Pre-alloyed powder, which is primarily used in laser powder bed fusion (LPBF), has the disadvantages of requiring time and high manufacturing costs. To overcome these limitations, in-situ alloying, which mixes pure elemental powders and alloys them in real-time during the LPBF process, has attracted attention. In particular, manufacturing high entropy alloys (HEA) containing high-melting-point refractory elements through in-situ alloying presents considerable challenges. In this study, a non-equiatomic single body-centered cubic (BCC) solid-solution HEA was fabricated via in-situ alloying with Ti, Nb, Mo, Ta, and W powders through the LPBF process. Specifically, by applying a high volumetric energy density (VED), we successfully mitigated the segregation of constituent elements, leading to an enhanced crystallographic texture. Consequently, the reduction in the residual stress and high-angle grain boundary (HAGB) density progressed, contributing to an increased relative density. Thus, this study marks a pioneering endeavor for in-situ alloyed HEA fabrication via LPBF, illustrating the efficacy of in-situ alloying utilizing mixed powders.

1. Introduction

High-entropy alloys (HEAs) are characterized by their composition. HEAs are made up of 5–35 at.% of five or more principal elements [1], deviating from the conventional alloy paradigm of incorporating additional elements into one or two base elements. This distinctive feature imparts heightened design flexibility to HEAs [2], making them promising candidates for next-generation alloys because of their excellent mechanical properties and corrosion resistance [3–6]. Nevertheless, the intrinsic super-multicomponent nature of HEAs leads to unavoidable segregation. Given the paramount importance of the homogeneous distribution of the constituent elements, segregation can diminish the distinctive properties of HEAs. We employed laser powder bed fusion (LPBF) for tailored shape customization and to mitigate constituent element segregation through an ultra-high cooling rate (10^5–10^7 Ks^{-1}). Additionally, we explored the control of the mechanical properties by manipulating the crystallographic texture, and the usefulness of LPBF in fabrication was demonstrated [7,8].

In the context of LPBF, the conventional practice involves the utilization of pre-alloyed powder generated through gas atomization. However, this approach introduces notable challenges in terms of the increased time and cost associated with powder manufacturing, thereby imposing constraints on the design versatility of the alloy [9–11]. To circumvent the drawbacks inherent to pre-alloyed powders, the emerging technique of in-situ alloying, which involves real-time alloy formation during the LPBF process, has garnered attention [9–13]. The adoption of in-situ alloying obviates the necessity for pre-alloyed powder production, leading to a reduction in both time and cost. Moreover, using mixed powders in-situ alloying permits the amalgamation of pure elemental powders according to the specified alloy composition, thereby enhancing the design flexibility of HEAs [9–11].

Refractory elements (Ti, V, Zr, Nb, Mo, Hf, Ta, and W) have attracted considerable attention as integral components of HEAs. These elements demonstrate notable attributes, such as exceptional high-temperature resistance, enhanced mechanical strength, and biocompatibility, rendering them widely applicable in biomaterials [3,7,8,14–18].

* Corresponding author at: Division of Materials and Manufacturing Science, Graduate School of Engineering, Osaka University, 2-1, Yamadaoka, Suita, Osaka 565-0871, Japan.
E-mail address: nakano@mat.eng.osaka-u.ac.jp (T. Nakano).

https://doi.org/10.1016/j.mtla.2024.102241
Received 4 June 2024; Accepted 22 September 2024
Available online 26 September 2024

Although the prospect of incorporating refractory elements in HEAs using LPBF is being explored, the elevated melting points of refractory elements pose challenges in achieving uniform melting. Consequently, the LPBF process requires a high energy density, leading to increased residual stress and crack formation [19,20]. An excessive energy density induces the evaporation of constituent elements, forming a keyhole-shaped melt pool and resulting in porosity. Therefore, careful application of the appropriate energy density is imperative. Notably, the formidable melting points of refractory elements present a significant impediment to in-situ alloying. Mooraj et al. performed in-situ alloying of Ti-Zr-Nb-Ta; however, the segregation of the constituent elements persisted at the boundaries of the melt pool [12]. Particularly noteworthy is the scarcity of research on the in-situ alloying application of W, which has the highest melting point among the metallic elements.

Therefore, in this study, in-situ alloying was performed by mixing pure elemental powders of Ti, Nb, Mo, Ta, and W in non-equiatomic HEA to take advantage of LPBF while eliminating the disadvantages of the pre-alloyed powder. We utilized alloy design with thermodynamic parameters and CALPHAD to suppress the segregation of the constituent elements of HEA. The conditions of mixing enthalpy (ΔH_{mix}), atomic radius mismatch (δ), and melting point mismatch (ΔT_m) to form a single-phase solid solution were considered, and $Ti_1(NbMoTa)_2W_{0.5}$, which showed the smallest ΔT (liquidus – solidus temperature), valence electron concentration (VEC), and electronegativity ($\Delta\chi_{Allen}$) was selected. With this alloy design strategy, $Ti_1(NbMoTa)_2W_{0.5}$ HEA suppressed the segregation of constituent elements even in the as-cast state [21]. Our focus here is on examining the energy density, constituent element segregation, and defects and elucidating their interrelationships. Notably, to the best of our knowledge, no prior investigation has focused on in-situ alloying via LPBF involving W. This study represents a pioneering effort to fabricate in-situ alloyed HEAs using LPBF.

2. Materials and methods

2.1. Properties of elemental powders and mixing procedure

Ti powder was sourced from OSAKA Titanium Technologies, Japan; Nb powder was obtained from TANIOBIS GmbH, Germany; Mo powder was supplied by Avimetal AM, China; Ta powder was acquired from H. C. Starck, Germany; and W powder was procured from Toshiba Materials, Japan, each with purities exceeding 99.5 %. The particle size distribution of each powder was assessed using a Mastersizer 3000E instrument (Malvern Panalytical, UK). The mixed powders underwent a 12-hour mixing process in a rocking mixer (RM-10; Japan) to ensure uniform homogeneity.

2.2. LPBF fabrication

In this study, in-situ alloyed non-equiatomic TiNbMoTaW HEA specimens with dimensions of 5 mm (depth) × 5 mm (length) × 5 mm (height) were fabricated using an LPBF machine (EOS M290, EOS, Germany). The manufacturing process adopted a singular XY-scan strategy, in which the scanning direction was rotated by 90° between successive layers. The laser powers (P) and scan speeds (v) were 180 and 300 W and 400 and 800 mm/s. Notably, a consistent hatch space (d) of 0.08 mm and layer thickness (t) of 0.02 mm was maintained across all conditions (Table 1). Therefore, attention should be paid to narrow layer thicknesses. The narrow layer thickness is expected to provide additional melting opportunities for the unmelted powder and enable a uniform distribution of the constituent elements. Additionally, small t of 0.02 mm provides sufficient overlap between scan layers while providing thermal accumulation [22], which helps relieve residual stress [23]. The volumetric energy density (VED) for the given fabrication conditions is defined by Eq. (1).

Table 1
Abbreviations and corresponding laser power, scan speed, hatch space, layer thickness, and VED of in-situ alloyed HEA specimens fabricated by LPBF.

Abbreviations	Laser power [W]	Scan speed [mm/s]	Hatch space [mm]	Layer thickness [mm]	VED [J/mm^3]
VED100	180	800	0.08	0.02	140.6
VED200	180	400			281.3
VED300	200	400			312.5
VED400	300	400			468.8

$$VED = \frac{P}{vtd}\ \left[\mathrm{J}\,/\,mm^3\right] \quad (1)$$

The VED calculated using Eq. (1) was 140.6 J/mm^3 for the VED100, 281.3 J/mm^3 for the VED200, 312.5 J/mm^3 for the VED300, and 468.8 J/mm^3 for the VED400. After each fabrication, the powders were remixed for 12 h, and the same specimens were fabricated several times to ensure reproducibility. For comparison, a specimen fabricated via arc melting with the same composition as the in-situ alloyed HEA was chosen. Elements with a purity of 99.9 % were used (Ti, Nb, Mo, and Ta from Kojundo Chemical Lab Co., Ltd., Japan, and W from Nilaco Corporation, Japan). Mixed lumps of pure elements were fabricated by arc melting (ACM-S01, DIAVAC Ltd., Japan). The remelting process was repeated at least 10 times to ensure uniform melting.

2.3. Microstructure characterization

The relative densities of the specimens produced via in-situ alloying using LPBF were assessed using an optical microscope (OM; BX-60, Olympus, Japan) and subsequently analyzed using ImageJ software. The phases in the original powders and the in-situ alloyed samples were investigated using X-ray diffraction (XRD; r X' pert PRO, Philips, Netherlands) employing Cu Kα radiation. Microstructural features and crystallographic textures were investigated using a field-emission scanning electron microscope (FE-SEM; JIB-4610F, JEOL, Japan) equipped with an energy-dispersive X-ray spectrometer (EDS; X-MaxN, Oxford Instruments, UK) and an electron backscatter diffraction system (EBSD; NordlysMax3, Oxford Instruments, UK). Nanohardness measurements were conducted using a nanoindentation tester (ENT-1100, Elionix Corp., Japan) with a test load of 15 mN (P_{max}), employing a progressive loading rate of 1 mN/s and maintaining P_{max} for 100 s.

3. Results

Fig. 1(a) presents the results of the size distribution for the Ti, Nb, Mo, Ta, and W powders, and Fig. 1(b-f) shows the morphologies of the Ti, Nb, Mo, Ta, and W powders. Ti, Nb, Mo, and Ta powders had similar sizes (D_{50} = 24.4–34.9 μm), but W powder had a much smaller size (D_{50} = 8.1 μm). For W, a small powder size was chosen because of its higher melting point relative to those of the other constituent elements. Small-sized powders can create a high-density powder bed in LPBF and increase laser absorption [24–27]; thus, even though the W powder has a high melting point, uniform melting is expected. To ensure powder homogenization, a mixer was employed for 12 h, and the efficacy of the mixing process was validated using the EDS results (Fig. 1g1-g6).

Fig. 2 shows the OM images captured in the yz-plane for VED100, VED200, VED300, and VED400. For comparison, cross-sections of the as-cast samples obtained by arc melting were observed. The as-cast sample produced via arc melting exhibited a relative density of 99.7 %. In addition, pores and microcracks stemming from the arc-melting process were observed. The VED100 sample exhibited the lowest relative density (93.4 %). Conversely, VED200 and VED300, which is characterized by an elevated VED, displayed an increased relative density of 94.6 % and 95.4 %, respectively. Notably, VED400, representing the highest VED, exhibited a maximum relative density of 96.9

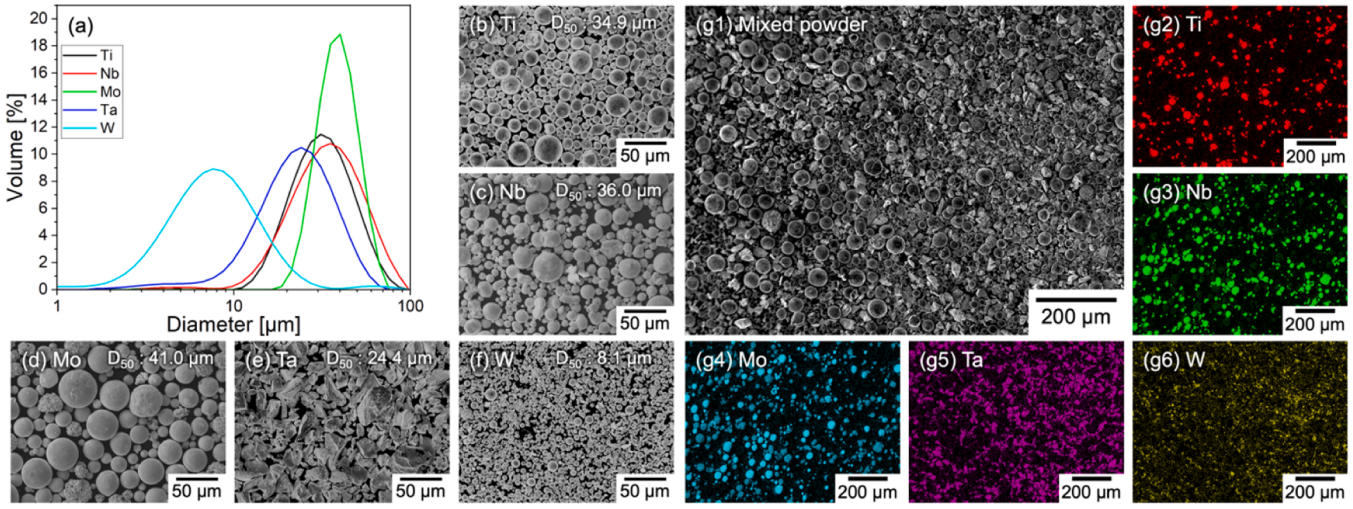

Fig. 1. (a) Size distribution of each powder: SEM image of (b) Ti powder; (c) Nb powder; (d) Mo powder; (e) Ta powder. (a) W powder. SEM image of the mixed powder (g1) and corresponding EDS maps (g2–6).

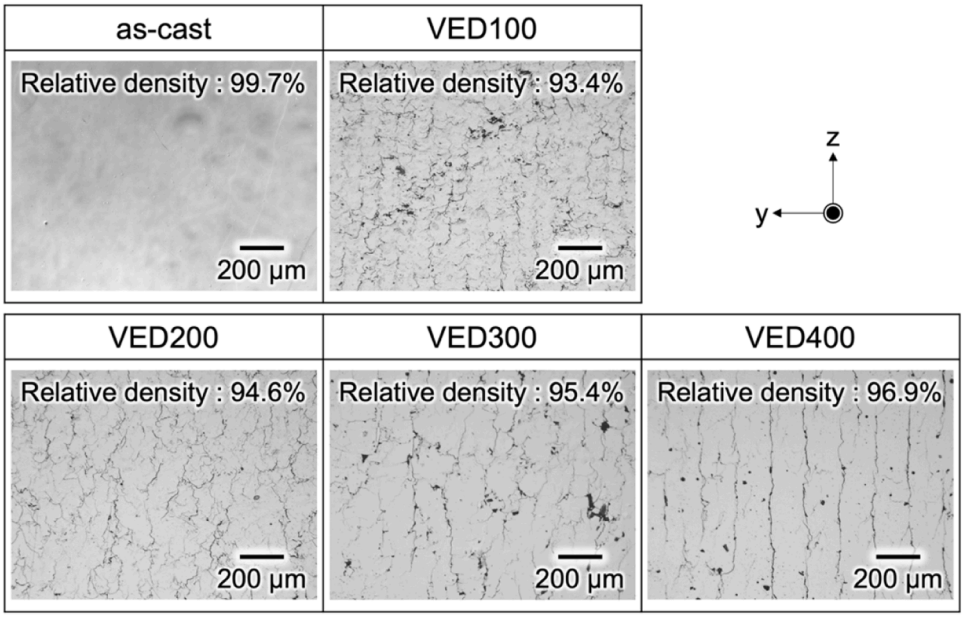

Fig. 2. OM images of the cross section for the yz-plane fabricated by in-situ alloying with LPBF and the as-cast sample.

%. Examination of the VED100 and VED200 samples revealed pronounced irregularities in crack propagation. However, with the increase of VED, transverse cracks were suppressed in VED300, and especially in the case of VED400 with the highest VED, most of the cracks were aligned along the building direction (BD, z-axis) with the suppression of transverse cracks. This behavior is attributed to the uniform distribution of elements and a concomitant reduction in residual stress resulting from a higher VED, which will be discussed in subsequent sections. Despite the observed increase in relative density with increasing VED, further investigations are warranted to achieve high-density in-situ alloyed HEAs.

Fig. 3 shows the XRD results for each individual elemental powder, the in-situ alloyed and as-cast samples. Fundamentally, all the in-situ alloyed HEAs and as-cast HEA exhibited a single body-centered cubic (BCC) structure. However, for VED100, an unmelted powder peak was evident. In contrast, in the instances of VED200, VED300, and VED400, no unmelted powder peaks were not detected. The full width at half maximum (FWHM) of the XRD peaks decreased with increasing VED (Table 2). The FWHM is intricately linked to the residual stress, homogeneity of constituent elements, and grain size. A narrower FWHM indicates a decrease in residual stress [28], more uniformly distributed constituent elements [29–31], and larger grain size [28,32]. Consequently, VED400, characterized by a high VED, exhibited the least residual stress, largest grain size, and suppressed segregation. The minimized FWHM observed in the as-cast sample can be attributed to the enlarged grain size resulting from the relatively slow cooling rate of arc melting. Furthermore, the discerned separation of observed peaks is ascribed to the decomposition of $K_{\alpha1}$ and $K_{\alpha2}$, not to the phase separation or formation of intermetallic compounds, as evidenced by the $K_{\alpha1}$ peak being approximately twice the intensity of the $K_{\alpha2}$ peak [28,32]. Furthermore, an observed peak shift to higher angles with increasing VED signifies a reduction in the lattice constant and achievement of a solid solution (Table 2). This suggests that the segregation of constituent elements in VED400, characterized by the largest 2θ, was effectively suppressed. This alignment with microstructural analyses, expounded upon subsequently, underscores the consistency of these findings, with

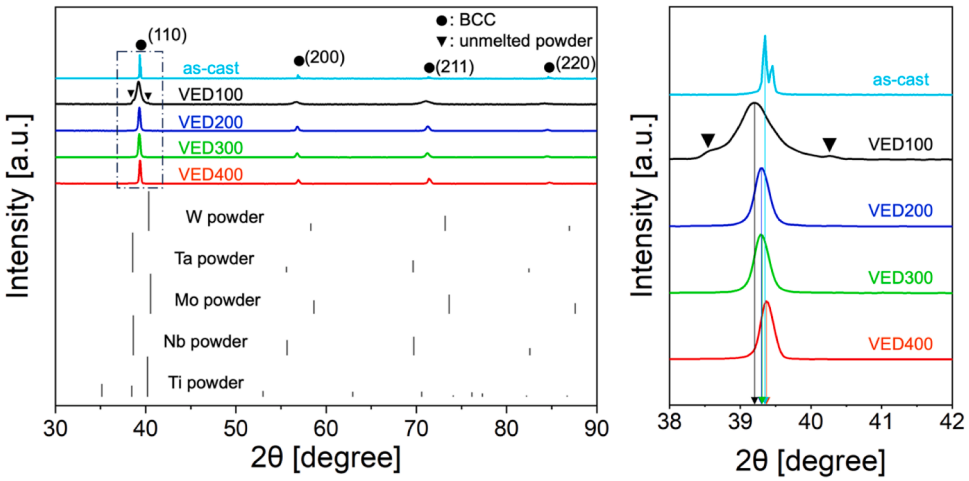

Fig. 3. XRD patterns of the as-cast sample by arc-melting, and VED100, VED200, VED300, and VED400 samples fabricated by LPBF with in-situ alloying and using each powder.

Table 2
The value of 2θ, FWHM, and lattice constants (a) of the (110) peak for in-situ alloyed HEA and as-cast HEA obtained through XRD measurements.

	2θ [°]	FWHM [°]	a [Å]
VED100	39.202	0.307	3.247
VED200	39.296	0.230	3.240
VED300	39.301	0.205	3.239
VED400	39.373	0.205	3.234
as-cast	39.349	0.094	3.236

further details to be elucidated in subsequent sections.

Fig. 4 shows backscattered electron (BSE) images obtained by SEM. The images illustrate the effect of the microstructure on VED, accompanied by the corresponding EDS mapping images from the in-situ alloyed and as-cast HEAs. The as-cast sample incorporated an alloy design to minimize the difference between the solidus and liquidus temperatures, thereby suppressing the segregation of the constituent elements, even under arc-melting conditions characterized by slow cooling rates (Fig. 4(a)). However, owing to differences in the melting points of the constituent elements, the dendritic regions exhibited an enrichment of high-melting-point elements (W and Ta), whereas the interdendritic regions displayed an abundance of low-melting-point elements (Ti, Nb, and Mo). In the case of VED100 (Fig. 4(b)), the EDS results can be confirmed by the unmelted powder and the element that was not entirely solid-solutionized. This phenomenon was attributed to the lack of laser energy to melt refractory elements with high melting points and insufficient mixing by Marangoni forces. For the VED200 samples (Fig. 4(c)), a notable impediment to elemental mixing was observed around the melt-pool boundary. Although VED300 showed a mostly uniform element distribution, segregation of constituent elements still existed (Fig. 4(d)). VED400, which was characterized by the highest VED (Fig. 4(e)), exhibited an increased energy density that was sufficient for the homogeneous melting of refractory elements with high melting points. The increased energy density increased the Marangoni force, substantiating the uniform distribution of the constituent elements throughout the melt pool [22]. The escalating VED correlates with suppressed element segregation, which is consistent with the XRD analysis results, thereby indicating enhanced uniformity of element incorporation. Additionally, it was observed that the segregation of constituent elements was suppressed in VED400 compared to the as-cast sample, and this was due to LPBF, which is characterized by a high cooling rate. This proves the effectiveness of in-situ alloying using a mixed powder. In the VED400, in contrast to the VED100, VED200, and VED300 the predominant alignment of cracks along the BD was observed in the central region of the melt pool, with a notable suppression of horizontal cracks. This behavior is attributed to the melt pool solidification mechanism starting from the side branches and ending at the center of the melt pool, forming high-angle grain boundaries and high-stress regions [33,34].

Fig. 5 shows the EBSD results corresponding to distinct process parameters, encompassing an inverse pole figure (IPF) map in the z-direction (Fig. 5(a1-d1)), a {100} pole figure (Fig. 5(a2-d2)), and a high-angle grain boundary (HAGB) map (Fig. 5(a3-d3)). In addition, the Kernel Average Misorientation (KAM) map (Fig. 5(a4-d4)), which measures the average misorientation between adjacent pixels to indicate residual stress [35,36], and the Taylor factor map (Fig. 5(a5-d5)), which indicates the efficiency of crystallographic shear to accommodate macroscopically enforced strain [37], are presented. Casting by arc melting shows a slower cooling rate than LPBF. Therefore, as-cast samples show a large average grain size with the random crystallographic texture compared to samples produced by LPBF, and thus a very low density of HAGB. In addition, the slow cooling rate was effective in relieving residual stress. VED100 exhibited the smallest average grain size and a random crystallographic texture (Fig. 5(b1, b2)). Conversely, with increasing VED, the average grain size and crystallographic texture increased (Fig. 5(c1-e1, c2-e2)). As the grain size increased, the density of HAGBs decreased (Fig. 5(b3-e3). In VED100, residual stress existed throughout the test specimen (Fig. 5(b4)), but as the VED increased, the residual stress decreased in VED200 and VED300 (Fig. 5(b4-d4)). Notably, in VED400, the residual stress was predominantly localized near cracks aligned in the BD (Fig. 5(e4)). A decrease in the Taylor factor with increasing VED was observed, indicative of enhanced ductility [38] (Fig. 5(b5-e5)).

Fig. 6 shows the correlations between the VED (a) and various parameters obtained from the EBSD analysis, including the average grain size (b), density of HAGB (c), averagekernel misorientation (d), average Taylor factor (e), and relative density (f) for in-situ alloyed HEA by LPBF. As the VED increased, the average grain size also increased. This means that epitaxial growth occurred as the VED increased. In the case of VED100, VED200, and VED300, epitaxial growth was impeded by the unmelted powders (Fig. 4). However, in VED400, where segregation was suppressed and a uniform solid solution was formed, epitaxial growth transpired across the molten pool, augmenting the crystallographic texture. The increase in the average grain size was concomitant with a decrease in the HAGB density (Fig. 5). Moreover, uniform melting mitigated the residual stress, leading to a reduction in the average misorientation. The segregation of the constituent elements was suppressed, uniform deformation was applied [39], and more deformation was accommodated, thereby reducing the Taylor factor. In essence, the

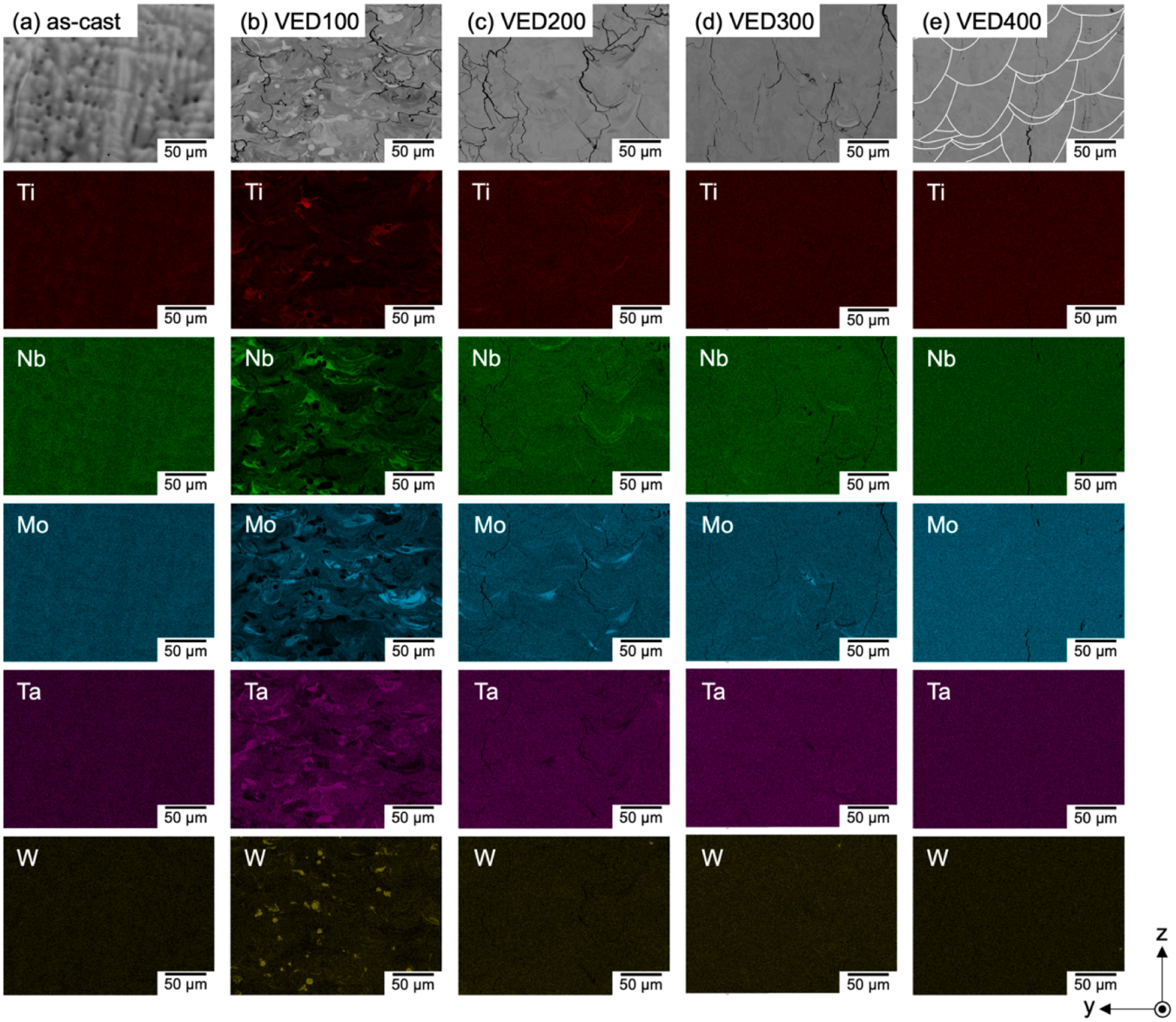

Fig. 4. SEM-BSE image of the (a) as-cast (b) VED100, (c) VED200, (d) VED300, (e) VED400 sample, and corresponding EDS maps.

elevation of the VED corresponds to the suppression of component segregation, reduction in HAGB density [40–42], and residual stress [43, 44], which are primary contributors to cracks in LPBF, resulting in increased relative density attributable to enhanced deformation accommodation.

4. Discussion

4.1. Sloid solution strengthening mechanisms

Fig. 7 shows the nanoindentation results for the as-cast HEA and the in-situ alloyed HEA. Nanoindentation was employed to mitigate the influence of defects such as cracks. VED100 showed the lowest nano-hardness, and as VED increased, nano-hardness increased, and base on this finding VED400 showed a significant increase in nano-hardness compared to VED100 and VED200 (Table 3). The nano-hardness of VED100 was expected to be higher than VED400 due to the Hall-Petch effect [45,46] owing to the small grain size and residual stress [47, 48], but the contradictory result was observed. This is thought to be due to the high relative density of the VED400 [49–51]. That is, the VED400, which showed the highest relative density in-situ alloyed HEA, showed the highest nano-hardness. In addition, the as-cast HEA showed significantly higher nano-hardness compared to VED100, VED200, and VED300 owing to higher relative density, but did not show significant difference than VED400, indicating that the increase in nano-hardness for LPBF-processed HEA was due to the increased relative density. In addition to the effect of relative density on nano-hardness, the solid solution strengthening (SSS) due to suppression of segregation of constituent elements also affected the strength of in-situ alloyed HEAs (Mo distribution inset in Fig. 7). HEAs are characterized by the inclusion of five or more primary elements in 5–35at.%, predominantly forming a random solid solution. Consequently, the incorporation of solute elements into solvents is a major means of enhancing the mechanical properties of HEAs, a phenomenon known as SSS [52]. The SSS effect ($\Delta\sigma$) was assessed using the model proposed by Senkov, which accounts for the interplay among atoms within HEAs characterized by a BCC structure [53]. The lattice parameter and shear modulus of pure elements used in this study are in Table 4. $\Delta\sigma$ is expressed as follows.

$$\Delta\sigma = A'G\delta^{4/3}c^{2/3} \tag{2}$$

where parameter A' is a dimensionless constant intrinsic to the material

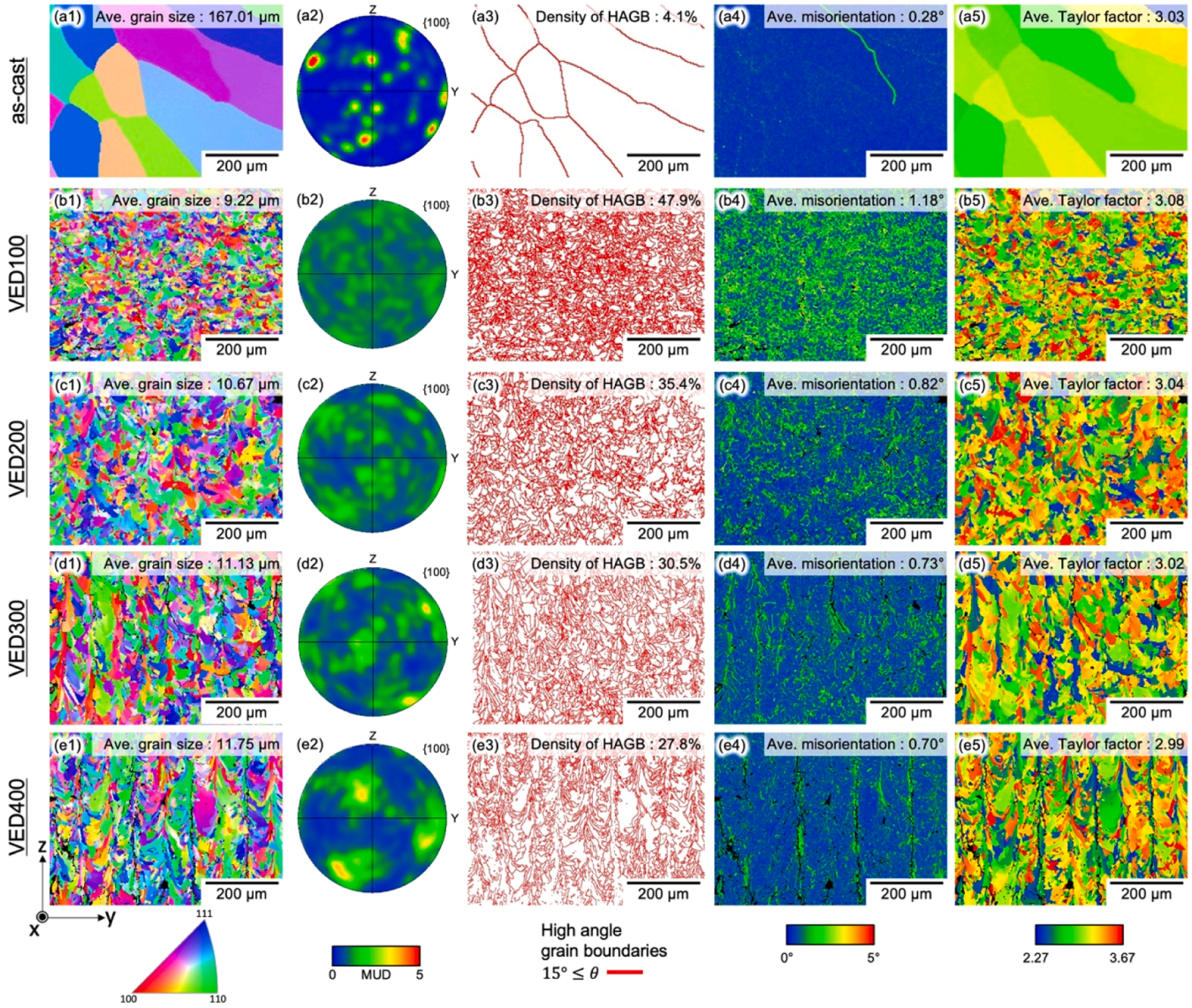

Fig. 5. (a1-e1) The IPF maps along BD and (a2-e2) {100} pole figures of the yz-plane orientation in the Z-direction. (a3-e3) Corresponding high angle grain boundary maps, (a4-e4) the kernel average misorientation maps, and (a5-e5) the Taylor factor maps.

and typically assumes values on the order of 0.1 [54]. G and c represent the shear modulus of the alloy and atomic fraction of the element, respectively. δ can be expressed as follows:

$$\delta = \delta_G + \beta\delta_a \tag{3}$$

where δ_G and δ_a indicate the shear modulus ($\delta_G = (1/G)dG/dc$) and atomic size misfit ($\delta_a = (1/a)da/dc$) parameters, respectively. a means atomic radius. The constant β is contingent upon the nature of the mobile dislocation and varies according to dislocation type. Specifically, for screw dislocations, β typically falls within the range of 2–4, whereas for edge dislocations, it attains values ≥ 16 [55,56]. The lattice distortion (δ_{ai}) and modulus distortion (δ_{Gi}) of i-element is calculated by an average of the atomic size difference of neighnors j-element as follows:

$$\delta_{ai} = \frac{9}{8}\sum c_j\delta_{aij} \tag{4}$$

$$\delta_{Gi} = \frac{9}{8}\sum c_j\delta_{Gij} \tag{5}$$

where c_j means atomic fraction of the j-element. $\delta_{aij} = 2(r_i - r_j)/(r_i + r_j)$ and $\delta_{Gij} = 2(G_i - G_j)/(G_i + G_j)$ represent are indicating atomic size and shear modulus difference of elements i and j (Table 5). Table 6 shows the calculated δ_{ai}, δ_{Gi}, and $\Delta\sigma$ of the in-situ alloyed non-equiatomic TiNbMoTaW HEA. The high VED of VED400 sufficiently melted the high-melting-point refractory elements and suppressed segregation (Fig. 4 (c)). Thus, VED400, which formed a random solid solution, had an increased shear modulus misfit and atomic size misfit, and its nanohardness was improved by SSS (Table 6).

4.2. Crack initiation and propagation

Fig. 8 shows the SEM-BSE images of the cracks, along with the corresponding EDS mapping, KAM, and HAGB images of the VED100 and VED400 samples. In VED100, conspicuous segregation of the constituent elements is evident, which is primarily attributed to differences in melting points. The inadequacy of melting in certain regions results in the presence of a liquid metal, leading to the development of tensile stress/strain due to solidification and thermal shrinkage in the vicinity of the liquid film [57,58]. A crack occurs when the localized tensile stress surpasses the resistance of the material to cracking. This phenomenon is corroborated by the residual stress concentration at the

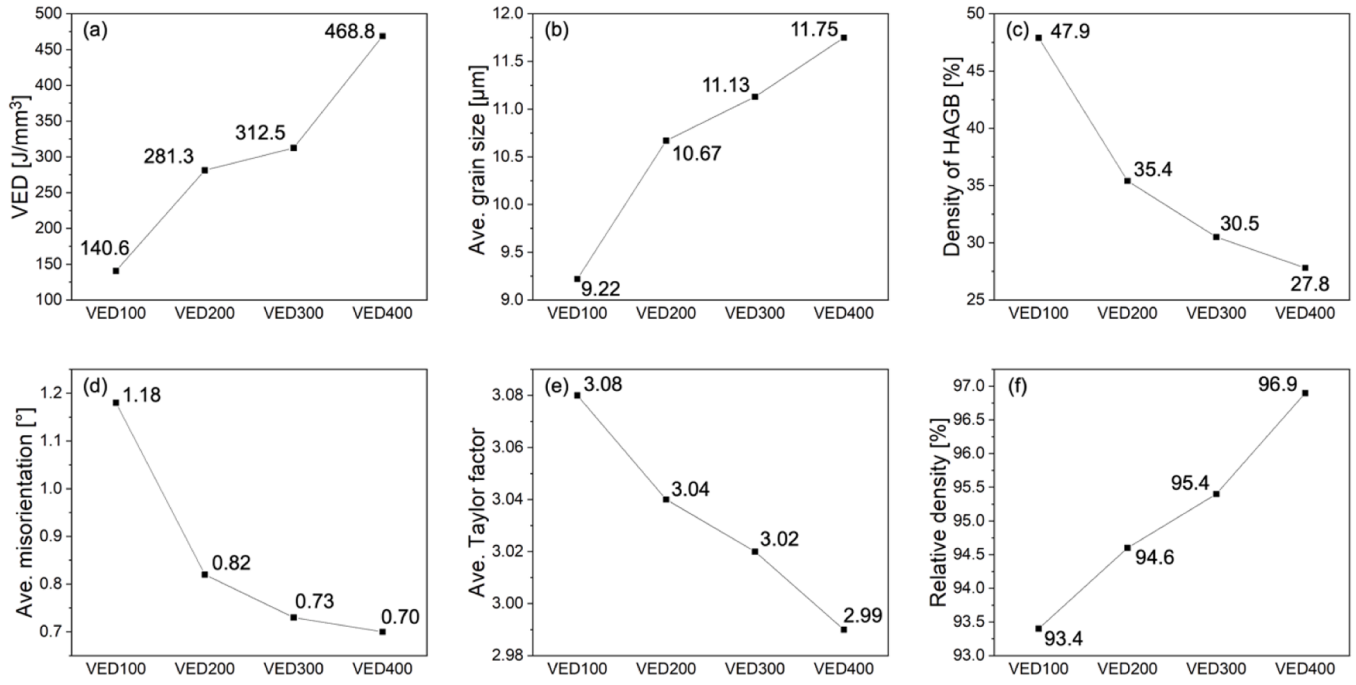

Fig. 6. Plot of (a) Volumetric energy density (VED), (b) Ave. grain size, (c) Density of HAGB, (d) Ave. misorientation, (e) Ave. Taylor factor and (f) Relative density from VED100, VED200, VED300, VED400 samples.

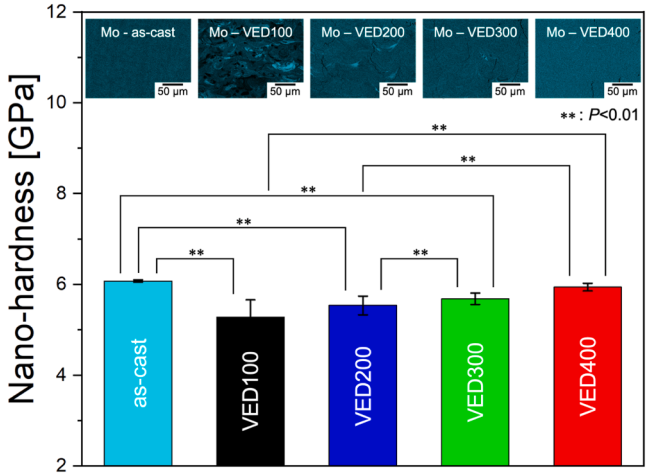

Fig. 7. Nano-hardness of as-cast HEA and in-situ HEAs in the average of 10 times measurement: **: $P < 0.01$ by Tukey's test.

Table 3
The nano-hardness of in-situ alloyed HEA and as-cast HEA.

	VED100	VED200	VED300	VED400	as-cast
Nano hardness [GPa]	5.3 ± 0.379	5.5 ± 0.205	5.7 ± 0.126	5.9 ± 0.084	6.1 ± 0.026

Table 4
The lattice parameter and shear modulus of pure elements.

	Ti	Nb	Mo	Ta	W
a [Å]	2.951	3.299	3.147	3.303	3.165
G [GPa]	45.6	37.5	125.6	69.2	160.6

Table 5
Atomic size difference (δ_{aij}, underlined numbers) and shear modulus difference (δ_{Gij}, bold numbers) of elements i and j.

$\delta_a ij$ / δ_{Gij}	Ti	Nb	Mo	Ta	W
Ti	0	**0.195**	**−0.935**	**−0.411**	**−1.115**
Nb	0.007	0	**−1.080**	**−0.594**	**−1.243**
Mo	−0.040	−0.047	0	**0.579**	**−0.245**
Ta	0.008	0.001	0.048	0	**−0.795**
W	−0.037	−0.044	0.003	−0.045	0

crack initiation site, which is discernible in the KAM map (arrows in Fig. 8(b)). Moreover, the formed crack propagated along the HAGB, which was prone to propagation (arrows in Fig. 8(c)) [40–42]. In contrast, in VED400, no noticeable segregation of the constituent elements was observed around the crack, resulting in a reduced residual stress distribution. Consequently, VED400 exhibited the suppression of transverse cracks, distinguishing it from VED100 and VED200. In VED400, the residual stress at the HAGB served as the crack initiation point, and the crack propagated along the HAGB, which is known for its susceptibility to cracking (arrows in Fig. 8(f)). Therefore, mitigating cracking and enhancing the relative density of in-situ alloyed HEA necessitates the reduction of residual stress and HAGB. Strategies, such as the relief of residual stress through elevated preheating [59,60] or heat accumulation [23], may prove beneficial. Consideration of HAGB reduction via enhanced crystallographic texture formation [42,61] or reduction of the scan length [62,63] is also noteworthy.

5. Conclusions

In this study, we fabricated non-equiatomic HEAs by LPBF using mixed powders of pure elements instead of pre-alloyed powders, which are time-consuming and costly to produce. The VED400 specimen exhibited homogeneous melting promoted by the elevated VED, resulting in the formation of a BCC solid solution with suppressed segregation of the constituent elements. Consequently, the residual stress issue was resolved by suppressed segregation, the average grain

Table 6
Calculated lattice distortion (δ_{ai}), shear modulus distortion (δ_{Gi}), and SSS effect ($\Delta\sigma$) of the in-situ alloyed non-equiatomic TiNbMoTaW HEA.

		Ti	Nb	Mo	Ta	W	$\Delta\sigma$ [MPa]
VED100	δ_{ai}	0.010	0.018	−0.033	0.019	−0.030	712.1
	δ_{Gi}	−0.328	−0.453	0.371	−0.039	0.520	
VED200	δ_{ai}	0.008	0.017	−0.036	0.017	−0.033	732.3
	δ_{Gi}	−0.296	−0.434	0.428	0.012	0.575	
VED300	δ_{ai}	0.010	0.019	−0.035	0.019	−0.031	778.6
	δ_{Gi}	−0.309	−0.445	0.410	−0.006	0.562	
VED400	δ_{ai}	0.012	0.020	−0.033	0.021	−0.030	808.8
	δ_{Gi}	−0.322	−0.456	0.397	−0.022	0.553	

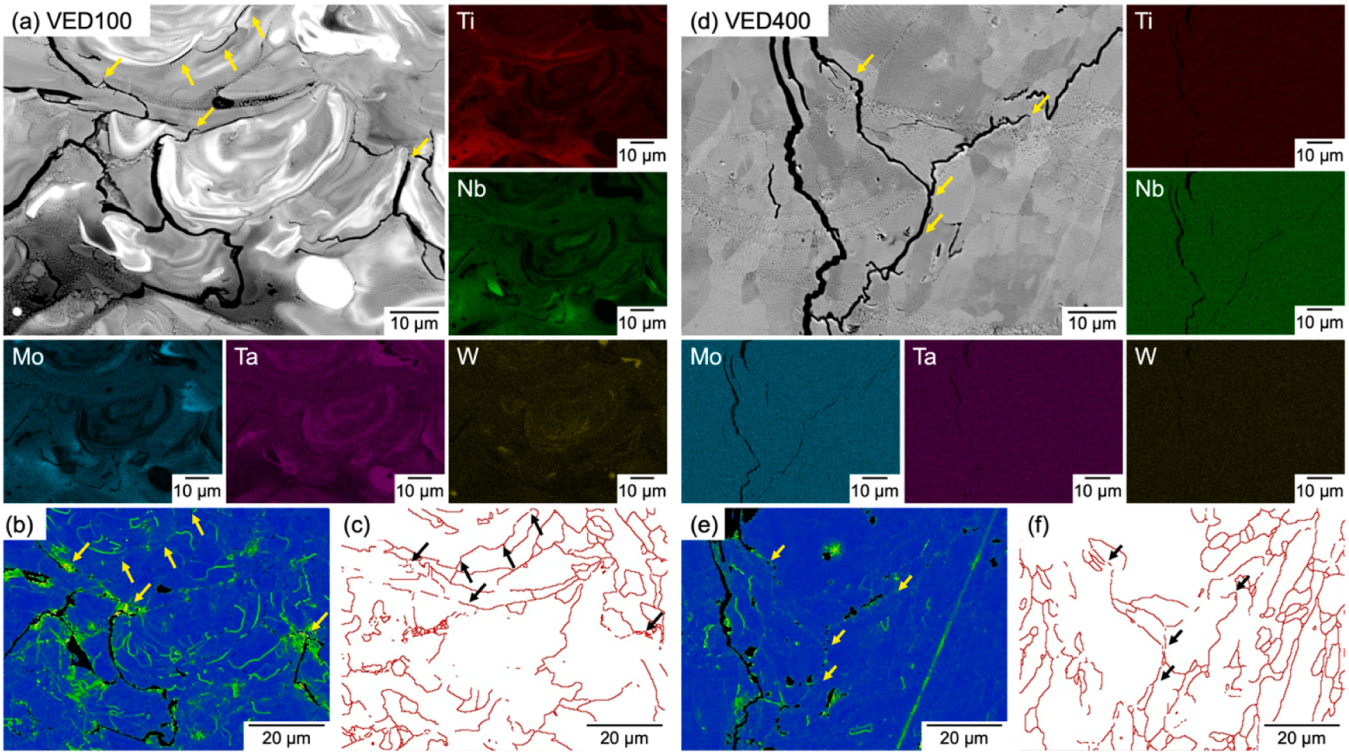

Fig. 8. SEM-BSE image and EDS mapping result of the (a) VED100 and (b) VED400 samples around the crack. Corresponding (b,e) kernel average misorientation maps and (c,f) high angle grain boundary maps by EBSD.

size increased owing to epitaxial growth while promoting texture development, and the HAGB density decreased, contributing to an elevated relative density. In addition, the formation of a random solid solution resulted in the highest nanohardness through SSS. Therefore, in-situ alloying in the LPBF process using a mixed powder is a promising method as it saves time and cost and enables the implementation of high design freedom. However, further research is required to overcome HAGB crack initiation and propagation; thus, studies are ongoing to promote single-crystal-like microstructures to prevent cracking.

CRediT authorship contribution statement

Yong Seong Kim: Writing – original draft, Visualization, Methodology, Investigation, Formal analysis, Conceptualization. **Ozkan Gokcekaya:** Writing – review & editing, Validation, Supervision, Methodology, Funding acquisition, Data curation, Conceptualization. **Aira Matsugaki:** Writing – review & editing. **Ryosuke Ozasa:** Writing – review & editing. **Takayoshi Nakano:** Writing – review & editing, Supervision, Project administration, Funding acquisition, Conceptualization.

Declaration of competing interest

The authors declare that they have no known competing financial interests or personal relationships that could have appeared to influence the work reported in this paper.

Acknowledgements

This work was supported by Grants-in-Aid for Scientific Research (JP23H00235 and JP24K07254) from the Japan Society for the Promotion of Science (JSPS) and CREST Nanomechanics: Elucidation of macroscale mechanical properties based on understanding the nanoscale dynamics of innovative mechanical materials (Grant Number: JPMJCR2194) from the Japan Science and Technology Agency (JST).

References

[1] J.W. Yeh, S.K. Chen, S.J. Lin, J.Y. Gan, T.S. Chin, T.T. Shun, C.H. Tsau, S.Y. Chang, Nanostructured high-entropy alloys with multiple principal elements: novel alloy design concepts and outcomes, Adv. Eng. Mater. 6 (5) (2004) 299–303, https://doi.org/10.1002/adem.200300567.

[2] Y. Ye, Q. Wang, J. Lu, C. Liu, Y. Yang, High-entropy alloy: challenges and prospects, Mater. Today 19 (6) (2016) 349–362, https://doi.org/10.1016/j.mattod.2015.11.026.

[3] M. Todai, T. Nagase, T. Hori, A. Matsugaki, A. Sekita, T. Nakano, Novel TiNbTaZrMo high-entropy alloys for metallic biomaterials, Scr. Mater. 129 (2017) 65–68, https://doi.org/10.1016/j.scriptamat.2016.10.028.

[4] Y. Zhang, T.T. Zuo, Z. Tang, M.C. Gao, K.A. Dahmen, P.K. Liaw, Z.P. Lu, Microstructures and properties of high-entropy alloys, Prog. Mater. Sci. 61 (2014) 1–93, https://doi.org/10.1016/j.pmatsci.2013.10.001.

[5] W.-R. Zhang, W.-B. Liao, P.K. Liaw, J.-L. Ren, J. Brechtl, Y. Zhang, Effects of transient thermal shock on the microstructures and corrosion properties of a reduced activation high-entropy alloy, J. Alloy. Compd. 918 (2022) 165762, https://doi.org/10.1016/j.jallcom.2022.165762.

[6] Y. Qiu, M. Gibson, H. Fraser, N. Birbilis, Corrosion characteristics of high entropy alloys, Mater. Sci. Technol. 31 (10) (2015) 1235–1243, https://doi.org/10.1179/1743284715Y.0000000026.

[7] O. Gokcekaya, T. Ishimoto, Y. Nishikawa, Y.S. Kim, A. Matsugaki, R. Ozasa, M. Weinmann, C. Schnitter, M. Stenzel, H.S. Kim, Y. Miyabayashi, T. Nakano, Novel single crystalline-like non-equiatomic TiZrHfNbTaMo bio-high entropy alloy (BioHEA) developed by laser powder bed fusion, Mater. Res. Lett. 11 (4) (2023) 274–280, https://doi.org/10.1080/21663831.2022.2147406.

[8] T. Ishimoto, R. Ozasa, K. Nakano, M. Weinmann, C. Schnitter, M. Stenzel, A. Matsugaki, T. Nagase, T. Matsuzaka, M. Todai, Development of TiNbTaZrMo bio-high entropy alloy (BioHEA) super-solid solution by selective laser melting, and its improved mechanical property and biocompatibility, Scr. Mater. 194 (2021) 113658, https://doi.org/10.1016/j.scriptamat.2020.113658.

[9] M. Cagirici, P. Wang, F.L. Ng, M.L.S. Nai, J. Ding, J. Wei, Additive manufacturing of high-entropy alloys by thermophysical calculations and in situ alloying, J. Mater. Sci. Technol. 94 (2021) 53–66, https://doi.org/10.1016/j.jmst.2021.03.038.

[10] P. Chen, S. Li, Y. Zhou, M. Yan, M.M. Attallah, Fabricating CoCrFeMnNi high entropy alloy via selective laser melting in-situ alloying, J. Mater. Sci. Technol. 43 (2020) 40–43, https://doi.org/10.1016/j.jmst.2020.01.002.

[11] P. Chen, C. Yang, S. Li, M.M. Attallah, M. Yan, In-situ alloyed, oxide-dispersion-strengthened CoCrFeMnNi high entropy alloy fabricated via laser powder bed fusion, Mater. Des. 194 (2020) 108966, https://doi.org/10.1016/j.matdes.2020.108966.

[12] S. Mooraj, G. Kim, X. Fan, S. Samuha, Y. Xie, T. Li, J.S. Tiley, Y. Chen, D. Yu, K. An, Additive manufacturing of defect-free TiZrNbTa refractory high-entropy alloy with enhanced elastic isotropy via in-situ alloying of elemental powders, Commun. Mater. 5 (1) (2024) 14, https://doi.org/10.1038/s43246-024-00452-0.

[13] T. Nagase, T. Hori, M. Todai, S.-H. Sun, T. Nakano, Additive manufacturing of dense components in beta-titanium alloys with crystallographic texture from a mixture of pure metallic element powders, Mater. Des. 173 (2019) 107771, https://doi.org/10.1016/j.matdes.2019.107771.

[14] S.-P. Wang, J. Xu, TiZrNbTaMo high-entropy alloy designed for orthopedic implants: as-cast microstructure and mechanical properties, Mater. Sci. Eng. C 73 (2017) 80–89, https://doi.org/10.1016/j.msec.2016.12.057.

[15] A. Hynowska, A. Blanquer, E. Pellicer, J. Fornell, S. Suriñach, M.D. Baró, S. González, E. Ibáñez, L. Barrios, C. Nogués, Novel Ti–Zr–Hf–Fe nanostructured alloy for biomedical applications, Materials (Basel) 6 (11) (2013) 4930–4945, https://doi.org/10.1016/j.scriptamat.2016.10.028.

[16] A. Motallebzadeh, N.S. Peighambardoust, S. Sheikh, H. Murakami, S. Guo, D. Canadinc, Microstructural, mechanical and electrochemical characterization of TiZrTaHfNb and $Ti_{1.5}ZrTa_{0.5}Hf_{0.5}Nb_{0.5}$ refractory high-entropy alloys for biomedical applications, Intermetallics 113 (2019) 106572, https://doi.org/10.1016/j.intermet.2019.106572.

[17] G. Perumal, H.S. Grewal, M. Pole, L.V.K. Reddy, S. Mukherjee, H. Singh, G. Manivasagam, H.S. Arora, Enhanced biocorrosion resistance and cellular response of a dual-phase high entropy alloy through reduced elemental heterogeneity, ACS Appl. Bio Mater. 3 (2) (2020) 1233–1244, https://doi.org/10.1021/acsabm.9b01127.

[18] T. Nagase, M. Todai, T. Hori, T. Nakano, Microstructure of equiatomic and non-equiatomic Ti-Nb-Ta-Zr-Mo high-entropy alloys for metallic biomaterials, J. Alloy. Compd. 753 (2018) 412–421, https://doi.org/10.1016/j.jallcom.2018.04.082.

[19] A. Talignani, R. Seede, A. Whitt, S. Zheng, J. Ye, I. Karaman, M.M. Kirka, Y. Katoh, Y.M. Wang, A review on additive manufacturing of refractory tungsten and tungsten alloys, Addit. Manuf. 58 (2022) 103009, https://doi.org/10.1016/j.addma.2022.103009.

[20] P. Hou, S. Mooraj, V.K. Champagne, M.J. Siopis, P.K. Liaw, S. Gerasimidis, W. Chen, Effect of build height on temperature evolution and thermally induced residual stresses in plasma arc additively manufactured stainless steel, Metall. Mater. Trans. A 53 (2022) 627–639, https://doi.org/10.1007/s11661-021-06538-5.

[21] Y.S. Kim, R. Ozasa, K. Sato, O. Gokcekaya, T. Nakano, Design and development of a novel non-equiatomic Ti-Nb-Mo-Ta-W refractory high entropy alloy with a single-phase body-centered cubic structure, Scr. Mater. 252 (2024) 116260, https://doi.org/10.1016/j.scriptamat.2024.116260.

[22] C. Guo, S. Li, S. Shi, X. Li, X. Hu, Q. Zhu, R.M. Ward, Effect of processing parameters on surface roughness, porosity and cracking of as-built IN738LC parts fabricated by laser powder bed fusion, J. Mater. Process. Technol. 285 (2020) 116788, https://doi.org/10.1016/j.jmatprotec.2020.116788.

[23] C. Chen, Z. Xiao, Y. Wang, X. Yang, H. Zhu, Prediction study on in-situ reduction of thermal stress using combined laser beams in laser powder bed fusion, Addit. Manuf. 47 (2021) 102221, https://doi.org/10.1016/j.addma.2021.102221.

[24] Y. Hou, H. Su, H. Zhang, F. Li, X. Wang, Y. He, D. He, An integrated simulation model towards laser powder bed fusion in-situ alloying technology, Mater. Des. 228 (2023) 111795, https://doi.org/10.1016/j.matdes.2023.111795.

[25] K. Riener, N. Albrecht, S. Ziegelmeier, R. Ramakrishnan, L. Haferkamp, A. B. Spierings, G.J. Leichtfried, Influence of particle size distribution and morphology on the properties of the powder feedstock as well as of AlSi10Mg parts produced by laser powder bed fusion (LPBF), Addit. Manuf. 34 (2020) 101286, https://doi.org/10.1016/j.addma.2020.101286.

[26] A.B. Spierings, N. Herres, G. Levy, Influence of the particle size distribution on surface quality and mechanical properties in AM steel parts, Rapid Prototyping J 17 (3) (2011) 195–202, https://doi.org/10.1108/13552541111124770.

[27] Y. Yang, D. Gu, D. Dai, C. Ma, Laser energy absorption behavior of powder particles using ray tracing method during selective laser melting additive manufacturing of aluminum alloy, Mater. Des. 143 (2018) 12–19, https://doi.org/10.1016/j.matdes.2018.01.043.

[28] Y. Waseda, E. Matsubara, K. Shinoda. X-ray Diffraction crystallography: introduction, Examples and Solved Problems, Springer Science & Business Media, 2011. doi:10.1007/978-3-642-16635-8.

[29] T. Löffler, F. Waag, B. Gökce, A. Ludwig, S. Barcikowski, W. Schuhmann, Comparing the activity of complex solid solution electrocatalysts using inflection points of voltammetric activity curves as activity descriptors, ACS Catal 11 (3) (2021) 1014–1023, https://doi.org/10.1021/acscatal.0c03313.

[30] A. Roy, P. Sreeramagiri, T. Babuska, B. Krick, P.K. Ray, G. Balasubramanian, Lattice distortion as an estimator of solid solution strengthening in high-entropy alloys, Mater. Charact. 172 (2021) 110877, https://doi.org/10.1016/j.matchar.2021.110877.

[31] U. Ulmer, K. Asano, A. Patyk, H. Enoki, Y. Nakamura, A. Pohl, R. Dittmeyer, M. Fichtner, Cost reduction possibilities of vanadium-based solid solutions–microstructural, thermodynamic, cyclic and environmental effects of ferrovanadium substitution, J. Alloy. Compd. 648 (2015) 1024–1030, https://doi.org/10.1016/j.jallcom.2015.07.110.

[32] M.G. Norton, C. Suryanarayana, X-Ray diffraction: a Practical Approach, Springer, Boston, 1998, https://doi.org/10.1007/978-1-4899-0148-4_1.

[33] J. Al-Lami, T. Dessolier, S. Rogers, T. Pirzada, M.-S. Pham, Dislocation distribution, crystallographic texture evolution, and plastic inhomogeneity of Inconel 718 fabricated by laser powder-bed fusion, Adv. Eng. Mater. (2023), https://doi.org/10.1002/adem.202400524.

[34] O. Gokcekaya, T. Ishimoto, S. Hibino, J. Yasutomi, T. Narushima, T. Nakano, Unique crystallographic texture formation in Inconel 718 by laser powder bed fusion and its effect on mechanical anisotropy, Acta Mater 212 (2021) 116876, https://doi.org/10.1016/j.actamat.2021.116876.

[35] X. Min, S. Emura, X. Chen, X. Zhou, K. Tsuzaki, K. Tsuchiya, Deformation microstructural evolution and strain hardening of differently oriented grains in twinning-induced plasticity β titanium alloy, Mater. Sci. Eng. A 659 (2016) 1–11, https://doi.org/10.1016/j.msea.2016.01.105.

[36] X. Zhang, H. Andrä, S. Harjo, W. Gong, T. Kawasaki, A. Lutz, M. Lahres, Quantifying internal strains, stresses, and dislocation density in additively manufactured AlSi10Mg during loading-unloading-reloading deformation, Mater. Des. 198 (2021) 109339, https://doi.org/10.1016/j.matdes.2020.109339.

[37] C.N. Tomé, R.A. Lebensohn, Material Modeling With the Viscoplastic Self-Consis-Tent (VPSC) Approach, Elsevier, 2021, https://doi.org/10.1016/C2019-0-01217-4.

[38] A. Keshavarzkermani, R. Esmaeilizadeh, U. Ali, P.D. Enrique, Y. Mahmoodkhani, N.Y. Zhou, A. Bonakdar, E. Toyserkani, Controlling mechanical properties of additively manufactured hastelloy X by altering solidification pattern during laser powder-bed fusion, Mater. Sci. Eng. A 762 (2019) 138081, https://doi.org/10.1016/j.msea.2019.138081.

[39] K. Ming, L. Li, Z. Li, X. Bi, J. Wang, Grain boundary decohesion by nanoclustering Ni and Cr separately in CrMnFeCoNi high-entropy alloys, Sci. Adv. 5 (12) (2019) eaay0639, https://doi.org/10.1126/sciadv.aay0639.

[40] D. Wang, Z. Wang, K. Li, J. Ma, W. Liu, Z. Shen, Cracking in laser additively manufactured W: initiation mechanism and a suppression approach by alloying, Mater. Des. 162 (2019) 384–393, https://doi.org/10.1016/j.matdes.2018.12.010.

[41] O. Gokcekaya, N. Hayashi, T. Ishimoto, K. Ueda, T. Narushima, T. Nakano, Crystallographic orientation control of pure chromium via laser powder bed fusion and improved high temperature oxidation resistance, Addit. Manuf. 36 (2020) 101624, https://doi.org/10.1016/j.addma.2020.101624.

[42] O. Gokcekaya, T. Ishimoto, T. Todo, P. Wang, T. Nakano, Influence of powder characteristics on densification via crystallographic texture formation: pure tungsten prepared by laser powder bed fusion, Addit. Manuf. Lett. 1 (2021) 100016, https://doi.org/10.1016/j.addlet.2021.100016.

[43] J. Platl, S. Bodner, C. Hofer, A. Landefeld, H. Leitner, C. Turk, M.-A. Nielsen, A. G. Demir, B. Previtali, J. Keckes, Cracking mechanism in a laser powder bed fused cold-work tool steel: the role of residual stresses, microstructure and local elemental concentrations, Acta Mater 225 (2022) 117570, https://doi.org/10.1016/j.actamat.2021.117570.

[44] P. Pant, F. Salvemini, S. Proper, V. Luzin, K. Simonsson, S. Sjöström, S. Hosseini, R. L. Peng, J. Moverare, A study of the influence of novel scan strategies on residual stress and microstructure of ι-shaped LPBF IN718 samples, Mater. Des. 214 (2022) 110386, https://doi.org/10.1016/j.matdes.2022.110386.

[45] E. Hall, The deformation and ageing of mild steel: III discussion of results, Proc. Phys. Soc. Section B 64 (9) (1951) 747, https://doi.org/10.1088/0370-1301/64/9/303.

[46] N.J. Petch, The cleavage strength of polycrystals, J. Iron Steel Inst. 174 (1953) 25–28.

[47] M. Wang, E. Liu, Y. Du, T. Liu, W. Liao, Cracking mechanism and a novel strategy to eliminate cracks in TiAl alloy additively manufactured by selective laser melting, Scr. Mater. 204 (2021) 114151, https://doi.org/10.1016/j.scriptamat.2021.114151.
[48] J. Wang, H. Hong, A. Huang, X. Yang, R. Qian, C. Shang, New insight into the relationship between grain boundaries and hardness in bainitic/martensitic steels from the crystallographic perspective, Mater. Lett. 308 (2022) 131105, https://doi.org/10.1016/j.matlet.2021.131105.
[49] K. Liu, D. Gu, M. Guo, J. Sun, Effects of processing parameters on densification behavior, microstructure evolution and mechanical properties of W–Ti alloy fabricated by laser powder bed fusion, Mater. Sci. Eng. A 829 (2022) 142177, https://doi.org/10.1016/j.msea.2021.142177.
[50] C. Cepeda-Jiménez, F. Potenza, E. Magalini, V. Luchin, A. Molinari, M. Pérez-Prado, Effect of energy density on the microstructure and texture evolution of Ti-6Al-4V manufactured by laser powder bed fusion, Mater. Charact. 163 (2020) 110238, https://doi.org/10.1016/j.matchar.2020.110238.
[51] G. Xue, L. Ke, H. Liao, C. Chen, H. Zhu, Effect of SiC particle size on densification behavior and mechanical properties of SiCp/AlSi10Mg composites fabricated by laser powder bed fusion, J. Alloy. Compd. 845 (2020) 156260, https://doi.org/10.1016/j.jallcom.2020.156260.
[52] J.-W. Yeh, Physical metallurgy of high-entropy alloys, Jom 67 (10) (2015) 2254–2261, https://doi.org/10.1007/s11837-015-1583-5.
[53] O. Senkov, J. Scott, S. Senkova, D. Miracle, C. Woodward, Microstructure and room temperature properties of a high-entropy TaNbHfZrTi alloy, J. Alloy. Compd. 509 (20) (2011) 6043–6048, https://doi.org/10.1016/j.jallcom.2011.02.171.
[54] R. Labusch, A statistical theory of solid solution hardening, Phys. Status Solidi B-Basic Solid State Phys. 41 (2) (1970) 659–669, https://doi.org/10.1002/pssb.19700410221.
[55] R.L. Fleischer, Substitutional solution hardening, Acta Metall 11 (3) (1963) 203–209, https://doi.org/10.1016/0001-6160(63)90213-X.
[56] L. Gypen, A. Deruyttere, Multi-component solid solution hardening: part 1 Proposed model, J. Mater. Sci. 12 (1977) 1028–1033, https://doi.org/10.1007/BF00540987.
[57] J. Fu, H. Li, X. Song, M. Fu, Multi-scale defects in powder-based additively manufactured metals and alloys, J. Mater. Sci. Technol. 122 (2022) 165–199, https://doi.org/10.1016/j.jmst.2022.02.015.
[58] S. Kou, Solidification and liquation cracking issues in welding, Jom 55 (2003) 37–42, https://doi.org/10.1007/s11837-003-0137-4.
[59] B. Vrancken, R.K. Ganeriwala, A.A. Martin, M.J. Matthews, Microcrack mitigation during laser scanning of tungsten via preheating and alloying strategies, Addit. Manuf. 46 (2021) 102158, https://doi.org/10.1016/j.addma.2021.102158.
[60] I. Polozov, V. Sufiiarov, A. Kantyukov, N. Razumov, I. Goncharov, T. Makhmutov, A. Silin, A. Kim, K. Starikov, A. Shamshurin, Microstructure, densification, and mechanical properties of titanium intermetallic alloy manufactured by laser powder bed fusion additive manufacturing with high-temperature preheating using gas atomized and mechanically alloyed plasma spheroidized powders, Addit. Manuf. 34 (2020) 101374, https://doi.org/10.1016/j.addma.2020.101374.
[61] M.C. Lam, S.C. Lim, H. Song, Y. Zhu, X. Wu, A. Huang, Scanning strategy induced cracking and anisotropic weakening in grain texture of additively manufactured superalloys, Addit. Manuf. 52 (2022) 102660, https://doi.org/10.1016/j.addma.2022.102660.
[62] O. Gokcekaya, T. Ishimoto, T. Todo, R. Suganuma, R. Fukushima, T. Narushima, T. Nakano, Effect of scan length on densification and crystallographic texture formation of pure chromium fabricated by laser powder bed fusion, Crystals 11 (1) (2020) 9, https://doi.org/10.3390/cryst11010009.
[63] D. Wang, S. Wu, Y. Yang, W. Dou, S. Deng, Z. Wang, S. Li, The effect of a scanning strategy on the residual stress of 316L steel parts fabricated by selective laser melting (SLM), Materials (Basel) 11 (10) (2018) 1821, https://doi.org/10.3390/ma11101821.